



OPEN

Spin glass states in multicomponent layered perovskites

P. Pramanik¹, R. Clulow², D. C. Joshi¹, A. Stolpe^{2,3}, P. Berastegui², M. Sahlberg² & R. Mathieu¹

Temperature-dependent dc-magnetization and ac-susceptibility curves have been recorded for series of single and double layered *Ruddlesden-Popper* multicomponent perovskites with chemical formula A_2BO_4 and $A_3B_2O_7$, respectively, with (La, Sr) on A-sites and up to 7 different cations on the B-sites (Ti, Cr, Mn, Fe, Co, Ni, Cu). The phase purity and chemical homogeneity of the compounds were investigated by X-ray diffraction and energy dispersive X-ray spectroscopy. Independently of the composition, spin glassiness is observed in both systems. Scaling analyses suggest the materials undergo spin glass phase transitions at low temperatures. Yet, qualitative differences are observed between the single-layered and double-layered systems, which are discussed in the light of the spatial dimensionality and magnetic interaction in layered oxide perovskites.

Multicomponent materials in the form of alloys and oxides have drawn a lot of attention over the years due to their distinct structural traits and correlated possibilities for customizing functional characteristics^{1–9}. In a recent study, Rost et al. reported the possibility to combine five distinct cations in equi-atomic ratios to form a single-phase oxide system, which was defined as an “entropy-stabilized oxide” due to entropy-driven structural stabilization effect³. A more comprehensive term, “high-entropy oxides (HEOs)”, has been used to classify multi-cationic oxide systems; the systems’ configurational entropy $S_{\text{config}} (= R[y_i \ln y_i])$, where R and y_i stand for the Boltzmann constant and percentage of each component, respectively), serves as the basis for the more all-encompassing concept of entropy stabilization^{9–11}. As a result, by including many randomly distributed atoms on the same sites, the chemistry of entropy stability enables the creation of novel single-phased materials.

Numerous HEOs including spinel, fluorite, perovskite, and rock salt crystal structures, have so far been created and investigated in order to modify their functional properties^{12–15}. Jiang et al. were the first to describe a new family of multicomponent oxides with a perovskite structure⁵. Most of these materials show an antiferromagnetic/ferrimagnetic behavior^{12,16,17}. Witte and co-authors also reported magnetic frustration in the rare earth (RE) and transition metal (TM) based high entropy oxides due to competing ferromagnetic and antiferromagnetic interactions in addition to the predominant antiferromagnetic coupling¹². Spin glass states^{18,19} are known to be ubiquitous to magnetic perovskites, e.g. manganite perovskites²⁰, more so in the low dimensional ones²⁰. Because of the competing magnetic interactions between the sparsely dispersed cations, the magnetic order in HEOs is extremely complex. Spin glassiness could hence be expected from the complex mixture of cations in the lattice, yet no spin glass phase has been evidenced so far in those materials. Furthermore, little is known about the magnetic properties of lower dimensional multicomponent systems such as Ruddlesden-Popper perovskites with chemical formula $A_{n+1}B_nO_{3n+1}$ ($n = \infty$: ABO_3 , labelled here “113”; $n = 1$: A_2BO_4 , “214”; $n = 2$: $A_3B_2O_7$, “327”) ²¹, which are illustrated in Fig. 1. Only a few reports are available, and mainly dealing with dimensionality-related superconducting properties²².

Here we report the magnetic properties of single and double layered Ruddlesden-Popper perovskites, which were found to show dynamical magnetic behavior and undergo spin glass phase transitions at low temperatures. We discuss the magnetic behavior of the glassy phases in the light of the magnetic interaction in these low-dimensional systems.

¹Department of Materials Science and Engineering, Uppsala University, Box 35, 751 03 Uppsala, Sweden. ²Department of Chemistry - Ångström Laboratory, Uppsala University, Box 538, 751 21 Uppsala, Sweden. ³FSCN Research Centre, Surface and Colloid Engineering, Mid Sweden University, 851 70 Sundsvall, Sweden. ✉email: prativa9piitg@gmail.com; roland.mathieu@angstrom.uu.se

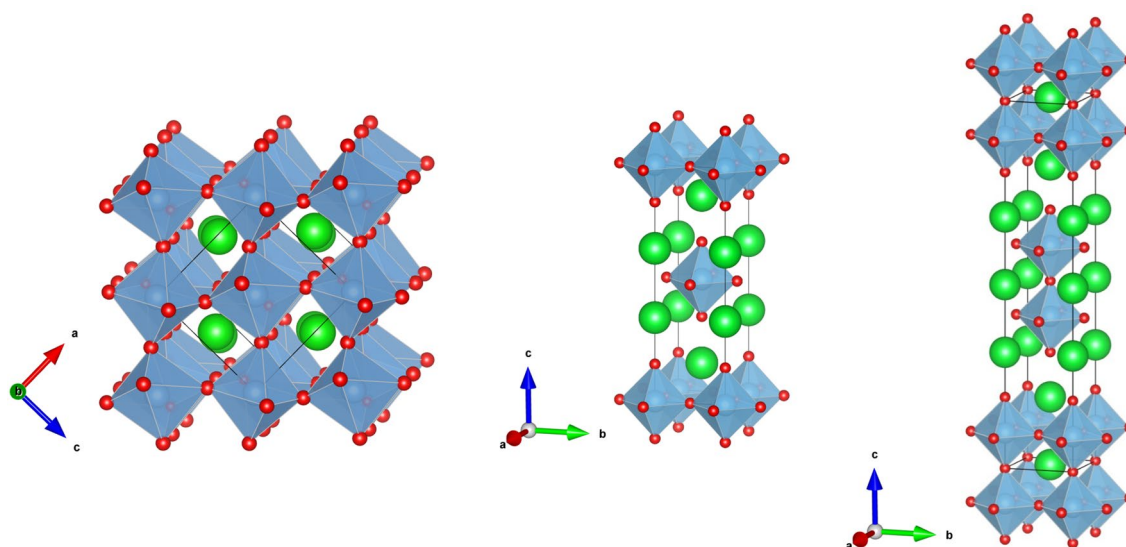


Figure 1. Polyhedral representations of the $A_{n+1}B_nO_{3n+1}$ perovskites: (left) $n = \infty$; ABO_3 , labelled here "113"; (middle) $n = 1$; A_2BO_4 , "214"; (right) $n = 2$; $A_3B_2O_7$, "327". Green spheres: non magnetic A-cations; blue: B-cations, red: oxygen anions; drawn using VESTA³⁶.

Results and discussion

The multicomponent perovskites were synthesized via a solid-state reaction method, as described in detail in Refs.^{17,23}. Two series of Ruddlesden-Popper perovskites consisting of single- and double-layer atomic arrangements, and chemical formulas A_2BO_4 , and $A_3B_2O_7$, respectively, were studied. B-sites are filled with up to seven different transition metal cations in order to increase the configurational tunability in term of ionic sizes and oxidation states¹⁷. La^{3+} and Sr^{2+} cations occupy the A-sites, and also affect the charge balance in the structure and the oxidation state of the B-site cations¹⁷. From here onwards the A_2BO_4 and $A_3B_2O_7$ family of samples will be referred to as 214, and 327, respectively. In each series, a total of four samples with different compositions were prepared, denoted 214_N and 327_N, respectively ($N = 1, 2, 3, 4$); details of the chemical composition and labels are summarized in Table 1. For comparison a multicomponent perovskite with chemical formula $La(Ti_{1/7}Cr_{1/7}Mn_{1/7}Fe_{1/7}Co_{1/7}Ni_{1/7}Cu_{1/7})O_3$ was prepared (labeled 113).

The crystal structure of the samples from each family were obtained from powder X-ray diffraction using the Rietveld refinement method (see Methods and supplementary Figs. SM1–SM3). The 113 sample adopts an orthorhombic structure with space group $Pnma$ while the 214 and 327 perovskites adopt a tetragonal crystal structure with $I4/mmm$ space group. The lattice parameters obtained from Rietveld refinements are listed in Table SM1. The lattice parameters obtained for the 113 sample are comparable to those reported earlier¹⁷. It is interesting to note that the c/a ratios between c - and a -axis lattice parameters are greater than 3 and 5 for the 214 and 327 series, respectively (see also Fig. 1). The surface morphology and individual elemental mapping for different atoms present in each phase were determined by the EDS analysis and are shown in Figs. SM7–SM8, respectively. The results of the EDS chemical compositional analysis obtained from ten various surface sites indicate average cationic compositions close to the expected nominal compositions, e.g. $LaSr_{1.04}(Ti_{0.13}Cr_{0.13}Mn_{0.15}Fe_{0.14}Co_{0.17}Ni_{0.14}Cu_{0.10})O_4$ and $La_{0.53}Sr_{2.47}(Mn_{0.52}Fe_{0.50}Co_{0.51}Ni_{0.48})O_7$, for $LaSr(Ti_{0.14}Cr_{0.14}Mn_{0.14}Fe_{0.14}Co_{0.14}Ni_{0.14}Cu_{0.14})O_4$ and $La_{0.5}Sr_{2.5}(Mn_{0.5}Fe_{0.5}Co_{0.5}Ni_{0.5})O_7$, respectively. EDS maps and results are given in the Supplemental Materials for a 214 phase (Figs. SM7 and SM8 and Table SM2); see Ref.⁹ for the 113 phase and Ref.²³ for the 327 ones.

Phase	Chemical formula	Label
$A(B)O_3$	$La(Ti_{1/7}Cr_{1/7}Mn_{1/7}Fe_{1/7}Co_{1/7}Ni_{1/7}Cu_{1/7})O_3$	113
$A_2(B)O_4$	$LaSr(Ti_{1/7}Cr_{1/7}Mn_{1/7}Fe_{1/7}Co_{1/7}Ni_{1/7}Cu_{1/7})O_4$	214_1
	$LaSr(Ti_{1/7}Mn_{1/7}Fe_{3/7}Co_{1/7}Cu_{1/7})O_4$	214_2
	$LaSr(Ti_{1/7}Mn_{2/7}Fe_{1/7}Co_{1/7}Ni_{1/7}Cu_{1/7})O_4$	214_3
	$LaSr(Cr_{1/6}Mn_{1/6}Fe_{1/6}Co_{1/6}Ni_{1/6}Cu_{1/6})O_4$	214_4
$A_3(B_2)O_7$	$La_{0.5}Sr_{2.5}(Mn_{1/4}Fe_{1/4}Co_{1/4}Ni_{1/4})_2O_7$	327_1
	$La_{0.5}Sr_{2.5}(Mn_{1/5}Fe_{2/5}Co_{1/5}Ni_{1/5})_2O_7$	327_2
	$La_{0.5}Sr_{2.5}(Mn_{2/6}Fe_{2/6}Co_{1/6}Ni_{1/6})_2O_7$	327_3
	$La_{0.5}Sr_{2.5}(Ti_{1/5}Mn_{1/5}Fe_{1/5}Co_{1/5}Ni_{1/5})_2O_7$	327_4

Table 1. Compositions of the different samples and their labels.

The temperature-dependent zero-field-cooled (ZFC) and field-cooled (FC) magnetization $M(T)$ of the investigated 214 and 327 systems recorded in $H = 1000$ Oe is presented in Fig. 2. They all exhibit a cusp in the ZFC magnetization below 40 K, while the FC magnetization is found to slightly increase with decreasing temperature; more significantly in the 214 case. No magnetic irreversibility is observed above the cusp temperature. While the temperature onset of the cusp is different by several degrees, the ZFC/FC curves of all the 214 (resp. all the 327) samples are qualitatively similar, and thus rather independent of the composition. The FC magnetization data is plotted as the inverse susceptibility $H/M = 1/\chi$ vs T in Fig. 3 to investigate the Curie–Weiss behavior. A linear behavior was obtained in all cases down to the lowest temperatures above the cusp, suggesting a homogeneous magnetic response. Lower (in absolute values) Curie–Weiss temperatures θ_{CW} were obtained for the 214 phases (~ 0 – 7 K vs ~ 13 – 22 K for the 327 ones; see Table SM5). Note that here we have aimed at showing the qualitatively similar magnetic behavior of the samples (see $M(T)$ or $\chi(T)$ curves), relatively independently of their composition, rather than correlating the values of the Curie–Weiss temperatures and associated effective moments to compositions; those parameters are listed in Table SM3. Magnetic field dependent $M(H)$ data was also collected and is shown for reference in the Supplemental Materials (Fig. SM10). The magnetic behavior evidenced by the ZFC/FC curves in Fig. 2 is reminiscent to that of spin glasses^{18,19,24}. Interestingly such spin glass states are ubiquitous in layered perovskites such as layered manganites^{20,25}. However, in order to evidence magnetic glassiness, and a low-temperature spin glass state, it is important to evidence that the material displays typical glassy characteristics such as aging, memory, and rejuvenation^{18,24} at low temperatures, and undergoes a spin glass phase transition^{18,20}.

If a spin glass is quenched from a temperature above its spin glass phase transition temperature T_g to a halt temperature below T_g in the glassy phase, and kept at that temperature for a certain time, the spin configuration established during cooling will slowly equilibrate by rearranging itself, or age²⁴. Interestingly, this aging may at

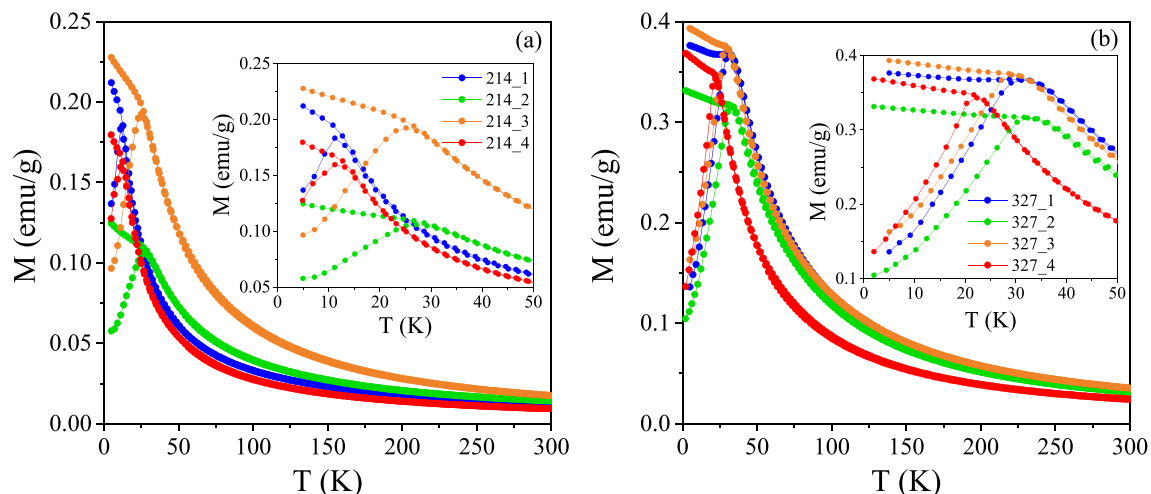


Figure 2. ZFC/FC magnetization M recorded in $H = 1000$ Oe for the (a) 214 and (b) 327 systems. The insets show the low-temperature behavior in more detail.

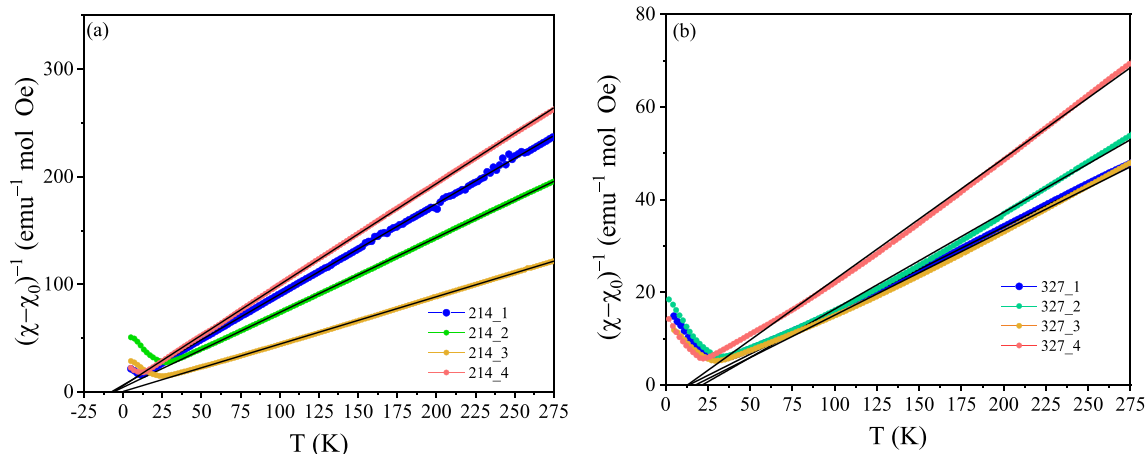


Figure 3. Temperature dependence of the inverse susceptibility $1/\chi = H/M$ vs T ($H = 1000$ Oe; filled markers) and linear fits (lines) for (a) 214 and (b) 327 systems, implying $\chi = C/(T - \theta_{CW}) + \chi_0$ (see Table SM3).

the same time be "kept in memory" by the system (memory feature) and forgotten (rejuvenation) on further temperature changes, as the spin configuration is rearranged on shorter length scales²⁴. This implies that if the system is further cooled down to a temperature far enough, it will appear rejuvenated (i.e. as if no aging had occurred), yet its aged configuration will be recovered upon reheating to the halt temperature²⁴. As a result, a relatively simple way to probe the glassy behavior, assuming magnetic fields low enough to provide a linear response, is to perform so-called memory experiments²⁴. In such experiments, the ZFC magnetization is first recorded on reheating in a small magnetic field after cooling the material from a reference temperature above T_g down to the lowest temperature (reference curve). The ZFC magnetization is then acquired one more time, now including a halt (or several) at a constant temperature T_h in the glassy phase for a certain halt time t_h , during the cooling to the lowest temperature (memory curve). In both cases, the magnetic field is always zero during the cooling and waiting. The aging at the halt temperature and subsequent rejuvenation on further cooling will have the memory curve coinciding with the reference curve at all temperatures but in the vicinity of T_h ; defining a "memory dip" in the (memory minus reference) difference curves¹⁷.

The ZFC/FC curves of two 214 and 327 systems recorded in a small field ($H = 25$ Oe) are shown in Fig. 4. The 327 phase display no irreversibility above the cusp temperature, while a slight irreversibility is observed for the 214 system, which may reflect a minor contribution from a secondary 113 phase (see Fig. SM2). Memory experiments were performed on both systems, including halts of $t_h = 1000$ s and 3000 s at $T_h = 20$ K. As seen in the insets of the Figure, both systems exhibit the characteristic memory dips associated with a glassy phase, and no significant features above the ZFC cusp temperature. In order to check whether the systems undergo a spin glass phase transition, ac-susceptibility measurements were performed and analyzed. First, it is interesting to note that spin glass-like ZFC/FC curves akin to those displayed by the 214 and 327 systems investigated here have not been observed in three dimensional (113) multicomponent perovskites. In the 113 systems which do not show a long ranged ferrimagnetic/antiferromagnetic order, ZFC/FC curves akin to those presented in Fig. SM9(a) have been reported^{17,26}, with a broad cusp in the ZFC magnetization, and magnetic irreversibility above the cusp temperature, even in relatively large magnetic fields (here 1000 Oe). This kind of magnetic behavior is often attributed to spin glass states, without further study¹⁸, and may instead reflect the magnetic inhomogeneity of the system, e.g. the inhomogeneous distribution of the magnetic cations on the B-site. As seen in Fig. SM9(b), memory dips are observed in the ZFC memory curves of the 113 sample recorded in a small magnetic field, indicating a glassy behavior. However the lack of well defined onset of non-equilibrium dynamics (e.g. a cusp, akin to that obtained in larger fields) suggests a lack of spin-glass phase transition, and hence that the observed dynamical magnetic behavior reflects the magnetic inhomogeneity of the system^{20,27}. Note that the 75–200 K region does not seem to be solely paramagnetic, considering the magnetization data in high and low magnetic fields presented in Fig. SM9 (a) and (b).

The ac susceptibility curves of selected 214 and 327 systems are shown in Fig. 5. The temperature and frequency dependence of those curves resemble those of spin glasses in both cases^{18,28}. $\chi''(\omega, T)$ curves "depart" from the equilibrium curve at lower and lower temperatures as the frequency of the ac excitation ($h = 4$ Oe, $f = \omega/2\pi = 0.51$ Hz to 510 Hz) decreases. This corresponds for $\chi''(\omega, T)$ to a frequency dependent onset which shifts accordingly in temperature^{18,28}. The onset of non-equilibrium is sharp in the 327 case, which suggests a spin glass phase transition. The cusp in the $\chi''(\omega, T)$ curves appear broader (and noisier due to the low magnetic signal) in the 214 case and the temperature onset of $\chi''(\omega, T)$ is not as sharp. A dynamical scaling analysis is performed in order to check the critical slowing down at the phase transition^{18,19}. Each frequency in the ac measurement defines a timescale, or observation time of the measurement, $\tau \sim 1/\omega$. Freezing temperatures T_f marking the onset of non equilibrium dynamics can be estimated from the susceptibility curves for each frequency, yielding (τ, T_f) datasets which, in case of a spin glass phase transition exhibit the power law $\tau = \tau_0 \varepsilon^{-z\nu}$ where $\varepsilon = (T_f - T_g)/T_g$ is the reduced temperature, z and ν critical exponents, and τ_0 reflects the microscopic flipping time of the interacting

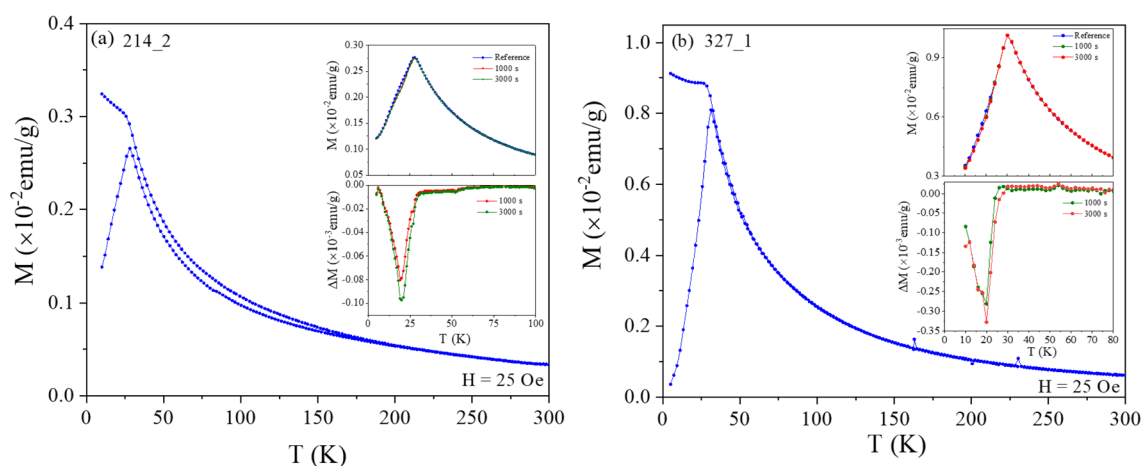


Figure 4. ZFC/FC magnetization recorded in $H = 25$ Oe for the (a) 214 and (b) 327 systems. The insets show the results of memory experiments: (top) ZFC magnetization recorded in $H = 25$ Oe with and without halts at $T = 20$ K in the cooling and (bottom) their corresponding difference curves ΔM versus T (curve with halt minus reference curve without halt).

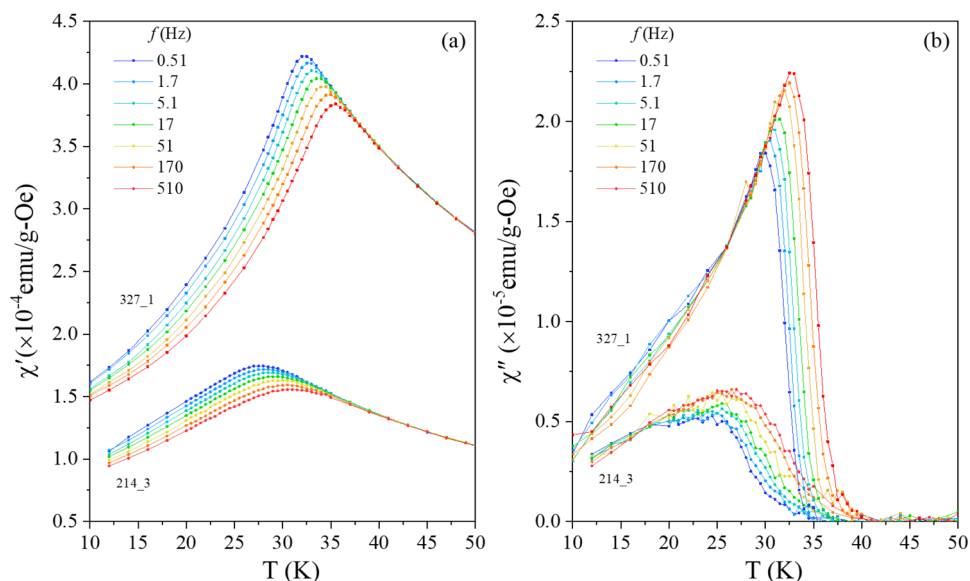


Figure 5. Temperature dependence of the (a) in-phase $\chi'(\omega=2\pi f;T)$ and (b) out-of-phase $\chi''(\omega,T)$ components of the ac-susceptibility for selected 214 and 327 samples recorded using a small ac-excitation $h=4$ Oe for different frequencies f .

entities^{18,28}. As seen in the main frame of Fig. 6, a relatively good scaling of the $\tau(\epsilon)$ is observed for both the 214 and 327 phases, yielding physical values of the $z\nu$ product and $\tau_0 : z\nu \sim 12 \pm 1$ both for 214 and 327 phases and $\tau_0 \sim 10^{-8 \pm 1}$ s for the 214 and $\sim 6 \times 10^{-11 \pm 1}$ s for the 327 phase, respectively ($T_g \sim 25 \pm 1$ K and 29 ± 1 K respectively), suggesting that the systems undergo a spin glass phase transition. While the obtained values of the $z\nu$ product are compatible with those of anisotropic spin glasses^{18,28} in the 10–12 range for both systems, the values of τ_0 are larger than that observed for model (atomic) spin glasses in the 214 case. Larger τ_0 values are typical for so-called superspin glasses, i.e. spin glasses in which the interacting entities are not single, atomic, spins, but superspins comprising several (many) coherently arranged spins; the amount determining the time scale of the fluctuation, i.e. τ_0 ²⁹. Such superspin glasses are often observed in strongly interacting magnetic nanoparticle systems²⁹, and have also been evinced in bulk systems whose magnetic state is build up of small (ferromagnetic) entities such as certain transition metal oxide perovskites²⁰; there $\tau_0 \sim 10^{-11 \pm 1}$ s (e.g. 113;³⁰ 214;^{20,31}).

In the 214 perovskites, spin glass states with lower (2D) spatial dimensionality have been observed³². Considering the 2D generalized Arrhenius scaling form for the slowing down, $\log(\tau/\tau_0) = T_f^{-(1+\psi\nu)}$ where ψ is another exponent^{20,32}, yields acceptable fits for the 214 phase, setting $\psi\nu$ to its "maximal" value of 1³²; implying $\tau_0 \sim 6 \times 10^{-13 \pm 1}$ s (see inset of Fig. 6). In the 2D case, the scaling form of the $\chi''(\omega,T)$ is relatively simple^{20,32} and

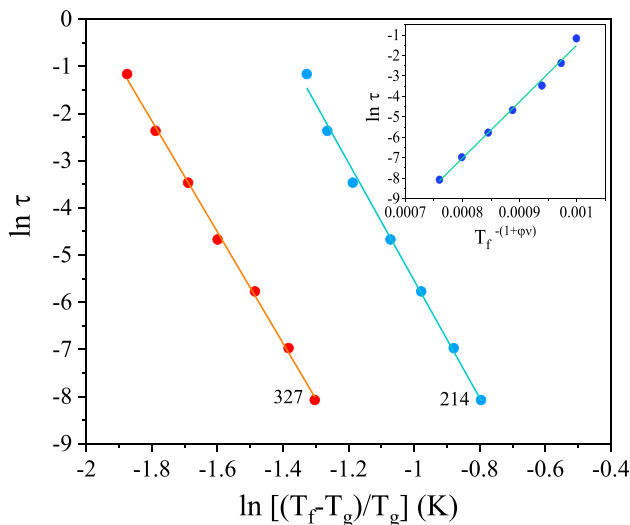


Figure 6. (3D) Scaling of τ with the reduced temperature $\epsilon = (T - T_g)/T_g$ for both 327 and 214 systems. A 2D scaling ($T_g=0$) is attempted in the inset for the 214 sample.

the full scaling of the $\chi''(\omega, T)$ data may be attempted³². As seen in Fig. SM12, a good scaling is observed for the 214 data using the values of ψv and τ_0 obtained from the $\tau(T_f)$ scaling.

Conclusions

The dynamical magnetic properties of two series of novel low-dimensional *Ruddlesden-Popper* multicomponent perovskites were investigated in detail. Zero-field cooled memory experiments evidence magnetic glassiness in both single layered (“214”) and double layered (“327”) systems at low temperatures. Scaling analyses of the ac-susceptibility suggest that both systems undergo a (3D) spin glass phase transition at a finite T_g , albeit qualitative differences can be observed between the 214 and 327 phases, possibly related to spatial dimensionality and magnetic interaction. In the 214 case, a reasonable scaling of the ac-susceptibility data is obtained considering a (2D) spin glass phase transition at $T_g = 0$ K.

Methods

The phase purity and crystal structure of all the sintered samples were determined by performing X-ray powder diffraction on a Bruker D8 ADVANCE diffractometer equipped with a Lynx-eye XE position sensitive detector (PSD) using CuK_α radiation ($\lambda = 1.5418 \text{ \AA}$). The diffraction patterns were collected at room temperature in the $10\text{--}100^\circ$ range in step of 0.014° . The data were analyzed using the Rietveld refinement method³³ within the Topas 6 program³⁴. Synchrotron X-ray diffraction data of the 214 samples were measured at the P02.1 beamline at PETRA III ($\lambda = 0.207 \text{ \AA}$). The data were recorded using a PerkinElmer XRD1621 fast area detector and integrated to a 1D diffraction pattern using the software Fit 2D³⁵. Polyhedral representations were drawn using VESTA³⁶. By collecting energy-dispersive X-ray spectroscopy (EDS) data from various locations on the sample surface, the elemental compositions of single-phase compounds were examined. Using a superconducting quantum interference device (SQUID) magnetometer from Quantum Design Inc., the dc-magnetization (M) and ac-susceptibility $\chi(\omega = 2\pi f, T)$ data was collected and used to analyze the static and dynamical magnetic properties of sintered pellets. In the ac experiments, frequencies (f) ranging from 0.51 to 510 Hz and ac excitation $h = 4$ Oe were employed. Furthermore, the aging and rejuvenation-like properties of selected samples were investigated by performing memory experiments following the dc-memory protocol²⁴. Magnetic field (H) dependent magnetization measurements for all samples were recorded at the lowest temperature.

Data availability

The datasets used and/or analysed during the current study available from the corresponding author on reasonable request.

Received: 12 November 2023; Accepted: 6 February 2024

Published online: 09 February 2024

References

- George, E. P., Raabe, D. & Ritchie, R. O. High-entropy alloys. *Nat. Rev. Mater.* **4**, 515 (2019).
- Ye, Y. F., Wang, Q., Lu, J., Liu, C. T. & Yang, Y. High-entropy alloy: Challenges and prospects. *Mater. Today* **19**, 349 (2016).
- Rost, C. *et al.* Entropy-stabilized oxides. *Nat. Commun.* **6**, 8485 (2015).
- Brahlek, M. *et al.* What is in a name: Defining “high entropy” oxides. *APL Mater* **10**, 110902 (2022).
- Jiang, S. *et al.* A new class of high-entropy perovskite oxides. *Scr. Mater.* **142**, 116–120 (2018).
- Wright, A. J. & Luo, J. A. A step forward from high-entropy ceramics to compositionally complex ceramics: A new perspective. *J. Mater. Sci.* **55**, 9812–9827 (2020).
- Oses, C., Toher, C. & Curtarolo, S. High-entropy ceramics. *Nat. Rev. Mater.* **5**, 295–309 (2020).
- Miracle, D. B. & Senkov, O. N. A critical review of high entropy alloys and related concepts. *Acta Mater.* **122**, 448–511 (2017).
- Bérardan, D., Franger, S., Dragoë, D., Meena, A. K. & Dragoë, N. Colossal dielectric constant in high entropy oxides. *Phys. Status Solidi Rapid Res. Lett.* **10**, 328 (2016).
- Bérardan, D., Franger, S., Meena, A. K. & Dragoë, N. Room temperature lithium superionic conductivity in high entropy oxides. *J. Mater. Chem. A* **4**, 9536 (2016).
- Zhou, J. *et al.* High-entropy carbide: A novel class of multicomponent ceramics. *Ceram Int.* **44**, 22014 (2018).
- Witte, R. *et al.* High-entropy oxides: An emerging prospect for magnetic rare-earth transition metal perovskites. *Phys. Rev. Mater.* **3**, 034406 (2019).
- Gild, J. *et al.* High-entropy fluorite oxides. *J. Eur. Ceram Soc.* **38**, 3578 (2018).
- Mao, A. *et al.* A new class of spinel high-entropy oxides with controllable magnetic properties. *J. Magn. Mater.* **497**, 165884 (2020).
- Sarkar, A. *et al.* Rare earth and transition metal based entropy stabilised perovskite type oxides. *J. Eur. Ceram Soc.* **38**, 2318 (2018).
- Witte, R. *et al.* Magnetic properties of rare-earth and transition metal based perovskite type high entropy oxides. *J. Appl. Phys.* **127**, 185109 (2020).
- Cedervall, J. *et al.* Phase stability and structural transitions in compositionally complex LnMO_3 perovskites. *J. Solid State Chem.* **300**, 122213 (2021).
- Nordblad, P. Competing interaction in magnets: the root of ordered disorder or only frustration. *Phys. Scr.* **88**, 058301 (2013).
- Kawamura, H. & Tanuguchi, T. Spin glasses. In *Handbook of Magnetic Materials* Vol. 24 (ed. Buschow, K. H. J.) 1–137 (Elsevier, Amsterdam, 2015).
- Mathieu, R. & Tokura, Y. The nanoscale phase separation in hole-doped manganites. *J. Phys. Soc. Jpn.* **76**, 124706 (2007).
- Evans, H. A., Mao, L., Seshadri, R. & Cheetham, A. K. Layered double perovskites. *Ann. Rev. Mater. Res.* **51**, 351–380 (2021).
- Mazza, A. R. *et al.* Searching for superconductivity in high entropy oxide Ruddlesden-Popper cuprate films. *J. Vac. Sci. Technol. A* **40**, 013404 (2022).
- Clulow, R., Pramanik, P., Stolpe, A., Joshi, D. C., Mathieu, R., Henry, P. F., & Sahlberg, M., Phase stability and magnetic properties of compositionally complex $n=2$ Ruddlesden Popper perovskites. *Submitted*.
- Mathieu, R., Jönsson, P., Nam, D. N. H. & Nordblad, P. Memory and superposition in a spin glass. *Phys. Rev. B* **63**, 092401 (2001).
- Mathieu, R. *et al.* Bandwidth-disorder phase diagram of half doped layered manganites. *Phys. Rev. B* **74**, 020404(R) (2006).

26. Pressley, L. A., Vivanco, H. K., Berry, T., Siegler, M. A. & McQueen, T. M. Transition metal (dis)order in single crystal multicomponent rare earth perovskites. *J. Cryst. Growth* **617**, 127262 (2023).
27. Mathieu, R., Nordblad, P., Nam, D. N. H., Phuc, N. X. & Khiem, N. V. Short range ferromagnetism and spin glass state in $Y_{0.7}Ca_{0.3}MnO_3$. *Phys. Rev. B* **63**, 174405 (2001).
28. Mathieu, R., Asamitsu, A., Kaneko, Y., He, J. P. & Tokura, Y. $Eu_{0.5}Sr_{1.5}MnO_4$: A three-dimensional XY spin glass. *Phys. Rev. B* **72**, 014436 (2005).
29. Hansen, M. F., Jönsson, P. E., Nordblad, P. & Svedlindh, P. Critical dynamics of an interacting magnetic nanoparticle system. *J. Phys. Condens. Matter* **14**, 4901 (2002).
30. Mathieu, R., Akahoshi, D., Asamitsu, A., Tomioka, Y. & Tokura, Y. Colossal magnetoresistance without phase separation: Disorder-induced spin glass state and nanometer scale orbital-charge correlation in half doped manganites. *Phys. Rev. Lett.* **93**, 227202 (2004).
31. Uchida, M. *et al.* Effect of random potential on charge-orbital-spin ordering in single layered manganites. *J. Phys. Soc. Jpn. Lett.* **75**, 053602 (2006).
32. Mathieu, R. *et al.* Logarithmic growth law in the two-dimensional Ising spin glass state resulting from the electron doping in single-layered manganites. *Phys. Rev. B* **76**, 014436 (2007).
33. Rietveld, H. M. A profile refinement method for nuclear and magnetic structures. *J. Appl. Cryst.* **2**, 65 (1969).
34. Coelho, A. A. TOPAS and TOPAS-Academic: an optimization program integrating computer algebra and crystallographic objects written in C++. *J. Appl. Cryst.* **51**, 210 (2018).
35. Hammersley, A. P., Svensson, S. O., Hanfland, M., Fitch, A. N. & Hausermann, D. *High Press. Res.* **14**, 235 (1996).
36. Momma, K. & Izumi, F. VESTA 3 for three-dimensional visualization of crystal, volumetric and morphology data. *J. Appl. Crystallogr.* **44**, 1272 (2011).

Acknowledgements

P.P. and R.M. thank Stiftelsen Olle Engkvist Byggmästare (Grant No. 207-0427) for financial support. The authors would like to acknowledge the support of the Swedish Foundation for Strategic Research (SSF, contract EM 160039) and Åforsk (contract 22-92). We acknowledge Myfab Uppsala for providing facilities and experimental support. Myfab is funded by the Swedish Research Council (2019-00207) as a national research infrastructure. We also acknowledge DESY (Hamburg, Germany), a member of the Helmholtz Association HGF, for provision of experimental facilities. Parts of this research were carried out at Petra III, and we would like to thank Dr Alexander Schökel for assistance in using the beamline P02.1.

Author contributions

Synthesis, chemical composition analyses and structural characterization were performed by R.C., A.S., P. B., and M.S. Magnetic property collection and analysis were performed by P.P., D.C.J., and R.M. All authors have jointly discussed the results and contributed to the final manuscript.

Funding

Open access funding provided by Uppsala University.

Competing interests

The authors declare no competing interests.

Additional information

Supplementary Information The online version contains supplementary material available at <https://doi.org/10.1038/s41598-024-53896-2>.

Correspondence and requests for materials should be addressed to P.P. or R.M.

Reprints and permissions information is available at www.nature.com/reprints.

Publisher's note Springer Nature remains neutral with regard to jurisdictional claims in published maps and institutional affiliations.



Open Access This article is licensed under a Creative Commons Attribution 4.0 International License, which permits use, sharing, adaptation, distribution and reproduction in any medium or format, as long as you give appropriate credit to the original author(s) and the source, provide a link to the Creative Commons licence, and indicate if changes were made. The images or other third party material in this article are included in the article's Creative Commons licence, unless indicated otherwise in a credit line to the material. If material is not included in the article's Creative Commons licence and your intended use is not permitted by statutory regulation or exceeds the permitted use, you will need to obtain permission directly from the copyright holder. To view a copy of this licence, visit <http://creativecommons.org/licenses/by/4.0/>.

© The Author(s) 2024